DSP-Based Implementation of a Real-time Sound Field Visualization System Using SONAH Algorithm

Zhe Zhang[1,2], Ming Wu[1,2] and Jun Yang[1,2]

[1] Institute of Acoustics, Chinese Academy of Sciences, No. 21 North 4th Ring Road, Haidian District, 100190 Beijing, China
[2] University of Chinese Academy of Sciences, No.19(A) Yuquan Road, Shijingshan District, 100049 Beijing, China
jyang@mail.ioa.ac.cn

Abstract. Many near-field acoustical holography (NAH) algorithms, including statistically optimized near-field acoustical holography (SONAH), have been well developed and verified via computer simulations. In this paper, design, implementation, and performance of a DSP-based real-time system for sound field visualization using SONAH algorithm is discussed. The prototype system consists of a 24-element microphone array connected to a TMS320C6678 DSP daughterboard hosted by a PC, validated by both computer simulation and experiments performed in an anechoic chamber, visualizing the sound field of a reconstruction plane in front of two speakers. The system has prospective practical applicability in industry applications.

Keywords: Digital signal processor (DSP), Statistically optimized near-field acoustical holography (SONAH), Microphone array.

1   Introduction

Statistically optimized near-field acoustical holography algorithm manages to avoid the errors and limitations of other NAH algorithms caused by using spatial DFT [1], also reducing the side-effects caused by the measuring aperture size of microphone array. During past twenty years, various SONAH algorithms in different coordinates based on sensor array were attempted to achieve higher resolution and higher robustness in various environments [2-6]. However, very few describe the actual implementation of acoustical holography system [7,8] and its use in practical real-time sound field visualization. There are also papers discussing the design, implementation, and performance of DSP system with microphone array for other purposes like DOA estimation and beamforming [9,10]. The system described in this paper uses TMS320C6678 multi-core digital signal processor as a core processor, cooperating with other associated hardware circuits. Taking advantages of the KeyStone multi-core architecture of the processor, the hardware and software are developed to run different tasks on different cores, thus providing a real-time performance of manipulating data and calculation of SONAH algorithm on a wide frequency band with low latency. After the reconstructed sound field were computed, the data were uploaded to

the host PC in a one-frame delay, which equals 16ms under a 16000Hz sampling rate and 256 samples buffer. The host PC then visualizes the reconstruction data. The prototype system is tested via computer simulation and experiments conducted in the free-field environments of an anechoic chamber.

Sound imaging techniques implemented by the system are becoming increasingly popular in various field, such as NVH problems in vehicle design, measuring of source positions, behavior, intensity and physical insight with details, evaluation of the performance of a speaker system, and so on. [11] There are also prospective applications in art field. Considering the more attention on "audiovisual" from visual and sound artists, the concept of "acoustic-visual" may be developed.

2 SONAH Algorithm

In this section, a brief review on SONAH algorithm [12] is presented with a data model adopted in following implementation.
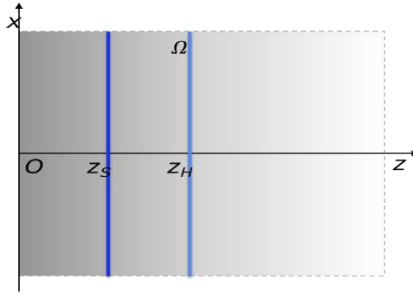
Fig. 1. Sound source and sound field in a SONAH model.

Consider a sound field reconstructing problem under free field condition. The surface of sound source is located at $z = z_S$ and region Ω is a source-free field occupied by air, shown as Fig. 1. According to the wave equation and spatial Fourier transform, sound pressure of a point $r = (x, y, z)$ can be represented as:

$$p(\mathbf{r}) = \frac{1}{4\pi^2} \iint P(k_x, k_y, z_s) e^{i[k_x + k_y + k_z(z - z_s)]} dk_x dk_y \qquad (1)$$

which indicating that sound pressure at point r can be represented as the sum a series of elementary waves propagating from the sound source $z = z_S$. Every elementary wave has its corresponding wave number vector and weighting coefficient and can be also represented as:

$$\Phi(\mathbf{k}, \mathbf{r}) = F(k_z) e^{i[k_x + k_y + k_z(z - z_s)]} \qquad (2)$$

where $\mathbf{k} = (k_x, k_y, k_z)$ is the wave-number vector and $F(k_z)$ is the amplitude weighting function. We can also see from Eq. (2) that $\Phi(\mathbf{k}, \mathbf{r})$ contains both the prop-

agation waves inside the radiation circle and the evanescent waves outside the radiation circle from the source.

Considering the amplitude weighting function $F(k_z)$, Hald J. proposes $F(k_z) = F_0\sqrt{1/|k_z|}$ as the "omni-directional weighting" [13], providing a better accuracy for sound waves with a large incident angles. In this paper, we choose the unit weighting, $F(k_z) = 1$, for the sake of experiment conditions discussed in next section.

Implement a wave-number domain sampling with Eq. (1) and Eq. (2), we yield:

$$p(\mathbf{r}) = \sum_n \frac{\Delta k_x \Delta k_y}{4\pi^2} P(\mathbf{k}_n, z_s)\Phi(\mathbf{k}_n, \mathbf{r}) \tag{3}$$

Then assume that the sound pressure on the holography plane $z = z_H$ has been measured at a set of positions. Apply Eq. (3):

$$p(\mathbf{r}_{Hj}) = \sum_n \frac{\Delta k_x \Delta k_y}{4\pi^2} P(\mathbf{k}_n, z_s)\Phi(\mathbf{k}_n, \mathbf{r}_{Hj}) \tag{4}$$

where

$$\mathbf{r}_{Hj} = (x_j, y_j, z_H) \quad (j = 1, 2, \cdots, M)$$

Similarly, according to the elementary wave model, the elementary waves at $\mathbf{r}$ can be represented as a linear combination of corresponding elementary waves at the sampling points on the holography plane [13]:

$$\Phi(\mathbf{k}_n, \mathbf{r}) = \sum_{j=1}^{M} c_j(\mathbf{r})\Phi(\mathbf{k}_n, \mathbf{r}_{Hj}) \tag{5}$$

where $c_j(\mathbf{r})$ is the weighting function of the elementary waves.

Combining Eq. (3), Eq. (4), and Eq. (5), we can yield:

$$p(\mathbf{r}) = \sum_{j=1}^{M} c_j(\mathbf{r})p(\mathbf{r}_{Hj}) = \mathbf{p}_H^T \mathbf{c}(\mathbf{r}) \tag{6}$$

which means that we can derive the sound pressure at $\mathbf{r}$ in Ω as long as we obtain the weighting function $c_j(\mathbf{r})$.

To calculate $c_j(\mathbf{r})$, rewrite Eq. (5) in the form of matrix:

$$\boldsymbol{\alpha}(\mathbf{r}) = \mathbf{A}\mathbf{c}(\mathbf{r}) \tag{7}$$

where

$$\boldsymbol{\alpha}(\mathbf{r}) = \begin{bmatrix} \Phi(\mathbf{k}_1, \mathbf{r}) \\ \Phi(\mathbf{k}_2, \mathbf{r}) \\ \vdots \\ \Phi(\mathbf{k}_{N-1}, \mathbf{r}) \end{bmatrix}, A = \begin{bmatrix} \Phi(\mathbf{k}_1, \mathbf{r}_{H1}) & \Phi(\mathbf{k}_1, \mathbf{r}_{H2}) & \cdots & \Phi(\mathbf{k}_1, \mathbf{r}_{HM}) \\ \Phi(\mathbf{k}_2, \mathbf{r}_{H1}) & \Phi(\mathbf{k}_2, \mathbf{r}_{H2}) & \cdots & \Phi(\mathbf{k}_2, \mathbf{r}_{HM}) \\ \vdots & \vdots & \ddots & \vdots \\ \Phi(\mathbf{k}_N, \mathbf{r}_{H1}) & \Phi(\mathbf{k}_N, \mathbf{r}_{H2}) & \cdots & \Phi(\mathbf{k}_N, \mathbf{r}_{HM}) \end{bmatrix}$$

Considering the Nyquist sampling condition and trade-off of the calculation load, the total sampling points for solve the equation is chosen as $N = (2N_x - 1)(2N_y - 1)$. Then we can derive from Eq. (7):

$$\mathbf{c}(\mathbf{r}) = \mathbf{A}^+ \boldsymbol{\alpha}(\mathbf{r}) \tag{8}$$

Thus, we can reconstruct the sound field in the field Ω with Eq. (6) and Eq. (8).

3 Implementation

3.1 Hardware Design

The block diagram of the developed prototype system is depicted in Fig. 2. The TMS320C6678 processor plays the center role in the real-time operations. The 24-channel ADC chip transforms analog signals captured by the microphone array with 24 elemental condenser microphones on the cross-points of 5x5 grid except for the bottom-right corner, shown in Fig. 3 (left). The distance between the nearest microphones in the array is 0.1125m. The DDR3 memory in the system makes it possible to store large floating number arrays of the coefficients downloaded from the host PC. The completed circuits board connected with the ADC chip is shown in Fig. 3 (right).
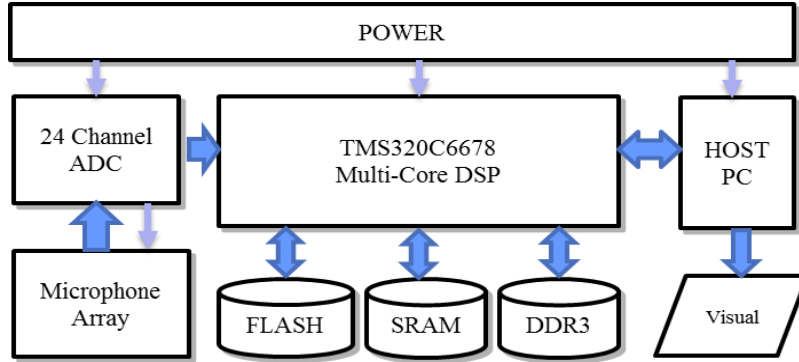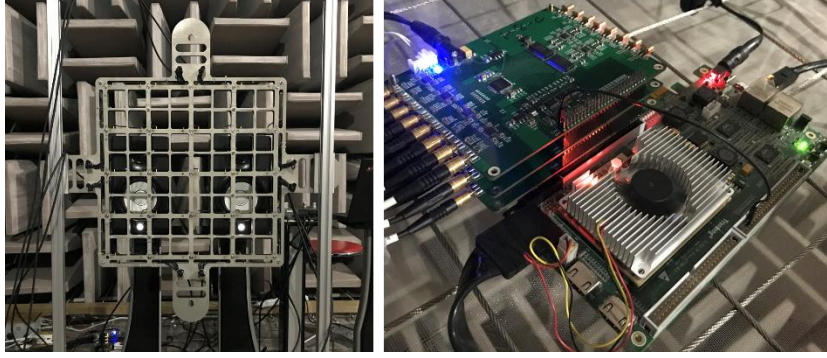

Fig. 2. Block diagram of the real-time sound field visualization system.

Fig. 3. The 24-channel microphone array (left) and the circuit board connected with the 24-channel ADC chip of the prototype system (right).

3.2 Software Development

Sound is captured by the microphone array and digitized by the ADC chip at the sampling rate of 16kHz. Thanks to the highly performance of the TMS320C6678 processor and its KeyStone multi-core architecture, the master core of the processor plays the role of data retrieval and communicating with host PC and simultaneously the slave cores fulfill the tasks of reading the coefficient block in the memory, manipulating matrices, and communicating with master core. Once the system starts to run, a 256-sample frame of data from each channel is gathered and an FFT with Blackman window is performed on all 24 channels in the master core. The master core then sends the FFT data in each frequency (up to the 8kHz in this 16kHz-sampling case) to the corresponding slave core that takes charge of that frequency. While the slave cores are manipulating the calculations of algorithms in current frame, the master core reads and sends the calculated results of last frame that the slave cores have finished to the host PC. Then the loop starts over again when the timer calls the master core to work on the next frame.

In addition, the reconstruction coefficients calculated from Eq. (7) may be large in data size, especially when the frequency range is big and/or the reconstruction resolution is high. Thus, we take the advantages of the mass storage of DDR3 and the high speed of RAM. The data block will be moved into RAM whenever the certain coefficient array is in need.

By implementing such software scheme, we guarantee that the system works in real-time with a low latency level: one-frame delay (16ms under the sampling rate and buffer size we use now). Anyway, there may also be latency caused by the analog-digital conversion and other process that should be taken into consideration in practical applications.

4   Performance

4.1   Computer Simulation

The SONAH algorithm described in Section 2 and prototype system described in Section 3 (except for the microphone array) were setup and run under the condition shown in Table 1.

Table 1. Computer Simulation Setup

z_S	z_H	Sound Source #1 on z_H	Sound Source #2 on z_H
$z_s = 0.1m$	$z_H = 0.15m$	(-0.1m, -0.1m)	(0.1m, 0.1m)

Two virtual sound sources were ideal point source located on the source plane $z = z_S$. The reconstruction plane was chosen as the same plane as the holography plane $z = z_H$ for the sake of convenience. The reconstruction resolution is set to 1cm, which means there will be 43*43 pixels on the visualization image.

The simulation results were shown in Fig. 4, visualizing the "true" value of the sound pressure and reconstruction value of the sound pressure on the reconstruction plane, respectively. In Fig. 5 (right), we plot two curve surfaces in the same coordinate to directly compare the results of reconstruction with the "true", which indicates a consistent trend of sound pressure distributing on the reconstruction plane.

Fig. 5 (left) shows the relative error of the reconstructing results compared with the "true" value. The maximum relative error is 30%, arising on the edge of the microphone array aperture. We find that when we choose a discrete representation in wave number domain in order to solve Eq. (5) and Eq. (7), the solutions will lead to wrap-around errors just like in traditional NAH based on spatial DFT processing.
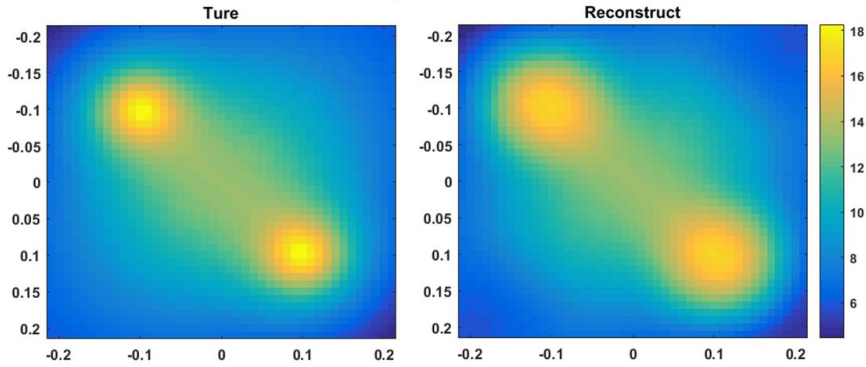
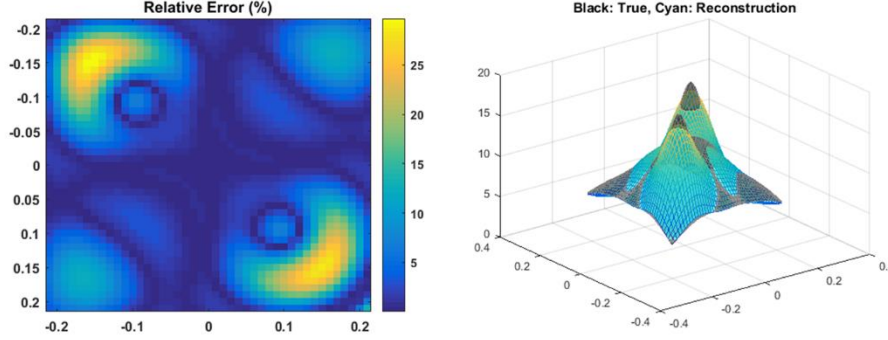**Fig. 4.** Computer simulation results.

Fig. 5. Relative error of reconstruction (left) and Sound pressure curve surface of "true" value and reconstructed value (right).

4.2 Experiment Results

The system has been tested in an anechoic room at Institute of Acoustics, Chinese Academy of Sciences. The whole setup of the experiment is shown in Fig. 6 (left). We use a pair of YAMAHA HS5 speakers as the sound source which is located in front of the microphone array. According to the Nyquist theorem:

$$2\pi / \Delta \geq 2k_{max} \tag{9}$$

Our microphone array with a sampling space of 0.1125m is capable for the max frequency:

$$f_{max} = c / 2\Delta = 1528.88Hz \tag{10}$$

Typically, the distance between sound source and holography plane satisfies $d \leq 0.5\lambda_{min}$ [14]. Considering the exponential decay of the evanescent wave and the low noise level in this case, we go slight far from it and set the distance $d = 0.1m$. The coordinate modeled based on the setup is shown in Fig. 6 (right). The speakers we use each has a woofer and tweeter taking charge of high frequency and low frequency, with a cross-point of 2kHz. Thus, we expected four sound sources in total if we drive the speakers using a signal up to 2kHz. The location of the centers of woofers and tweeters are depicted in Table 2. The reconstruction plane is coincided with the holography plane, same as the computer simulation.

Table 2. Experiment Setup

| Left Woofer	Left Tweeter	Right Woofer	Right Tweeter
(-0.17m, 0.06m)	(-0.17m, -0.09m)	(0.17m, 0.06m)	(0.17m, -0.09m)
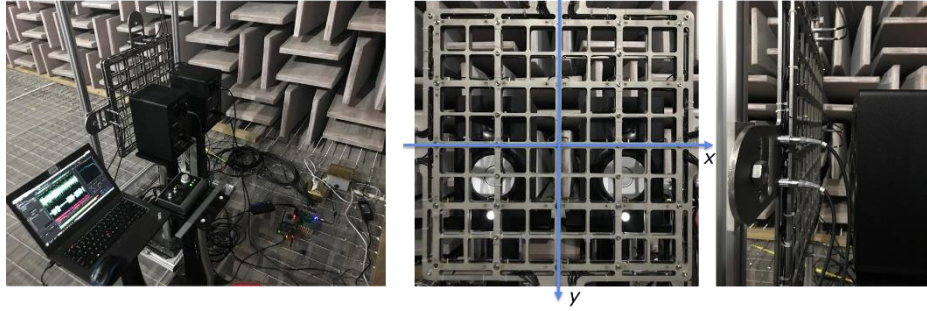
Fig. 6. Experiment setup and coordinates.

Fig. 7 shows the sound pressure distribution of 100Hz sine wave on the reconstruction plane. The top-left image is the distribution when only the speaker on the left makes sounds while the top-right image only the speaker on the right. The bottom-left image shows the sound pressure distribution on the reconstruction plane when the two speakers play the same in-phase sine wave, while the bottom-right image shows the out-of-phase situation. Fig. 8 and Fig. 9 also follow the same arrangement above, showing the distribution of 1000Hz and 2000Hz sine waves.

In our visualized reconstruction image, we can clear see the distribution of sound pressure in front of the speakers. The peak amplitudes show the positions of center of the corresponding sound sources. When the speakers work on low frequency such as 100Hz in Fig. 7 and 1000Hz in Fig. 8, only the woofer vibrates and radiates sounds. In addition, comparing the in-phase sine waves sound field and the out-of-phase ones, the interference phenomenon is captured by our system: in the bottom-left images there are strengthened bands in the center while in the bottom-right images that bands are weakened.

Although Eq. (10) tells that the prototype system has a cutoff frequency of about 1500Hz, we still go slightly far beyond that to test the system up to 2000Hz to see the expanding ability of it. Fig. 9 shows the reconstruction sound pressure of 2000Hz sine waves and Fig. 10 shows the reconstruction sound pressure in different layout of visualization of wide-band noise covering the frequency range of 60Hz-2000Hz, independent with each other from two speakers. We can see that the system still gets a good performance of orientation. And it meets our expectations that the speakers work on both woofer and tweeter when the frequency of the signal reaches the crosspoint 2000Hz.
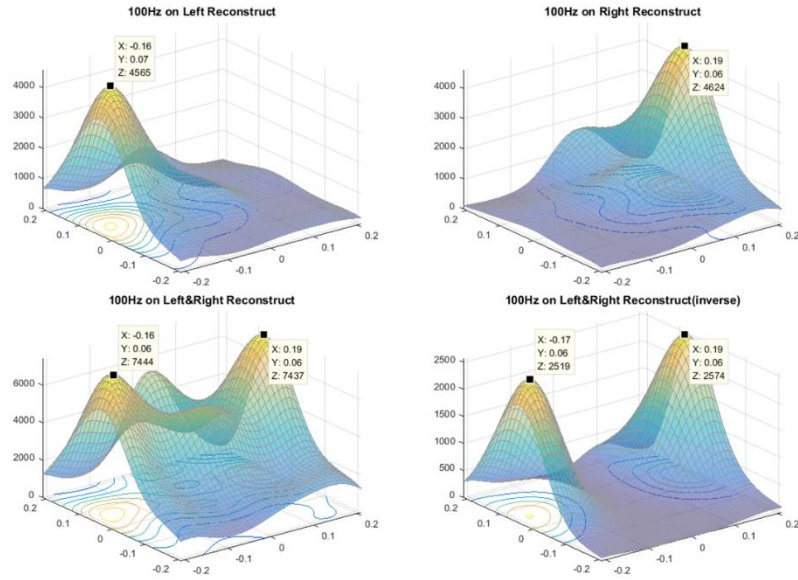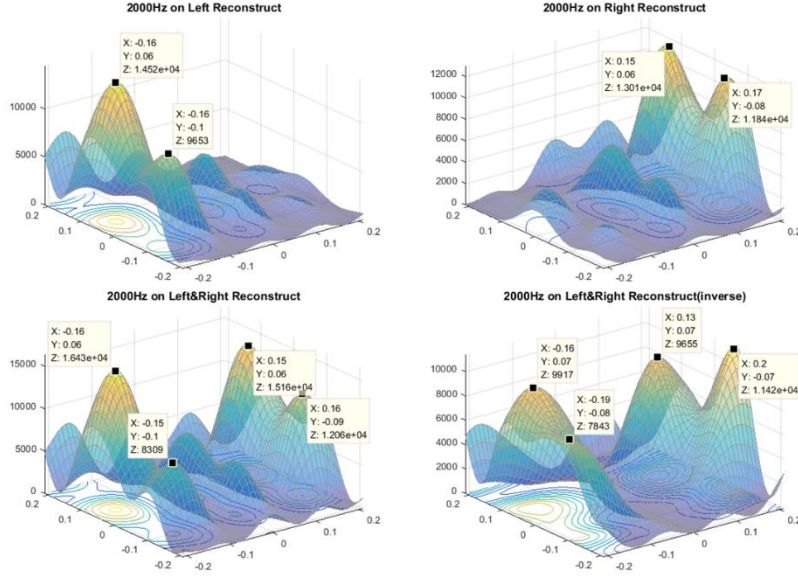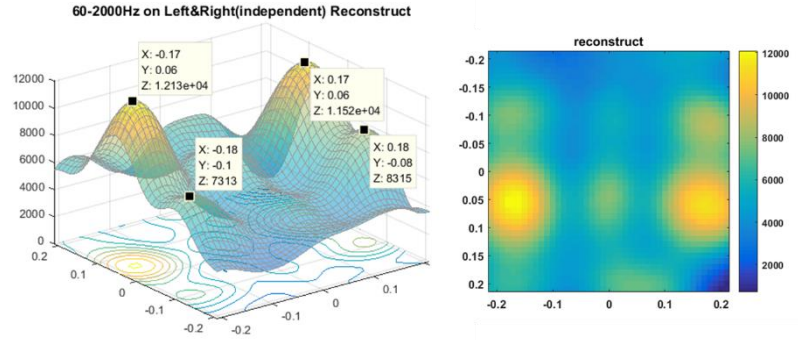
Fig. 7. Sound field visualization of 100Hz.
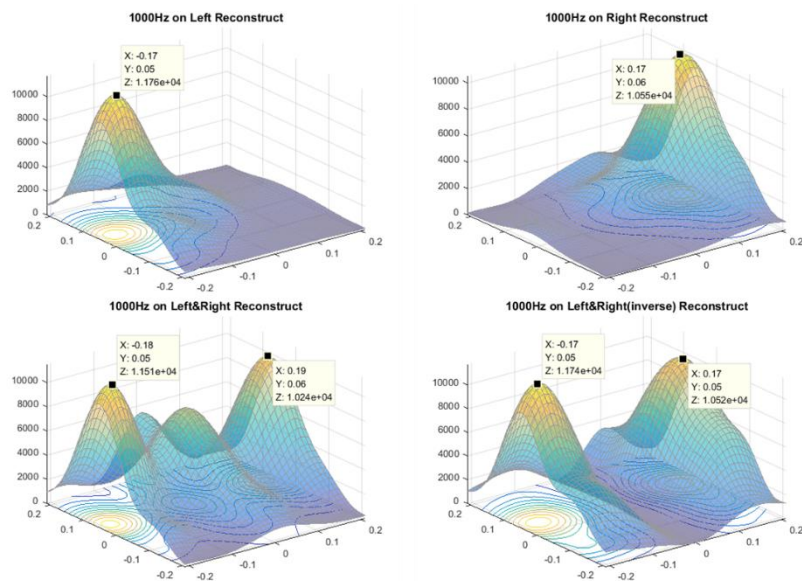
**Fig. 8.** Sound field visualization of 1000Hz.

Fig. 9. Sound field visualization of 2000Hz.

Fig. 10. Sound field visualization of independent wide-band noise (60Hz-2000Hz) .

Finally, we evaluate the accuracy of sound source localization of the prototype system in Fig. 11, where the "X" marks represent the true location of the sound source in Table 2. and the "O" marks represent the localization results of our system (some results fall on the same coordinates so that the marks overlap with each other). The maximum error of localization is less than 5cm and there may contain some measurement error due to the hands-on measuring and the vibration of the grid-floor of the anechoic chamber. The system performs better on low frequency than high frequency, which is also in line with our forecast.
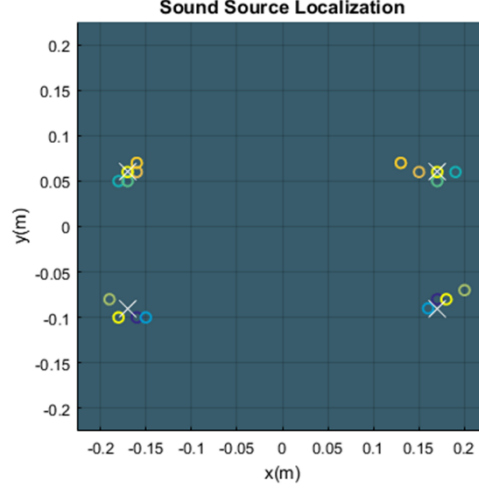
Fig. 11. Accuracy of sound source localization.

Additionally, we also carry out some test focusing on the dynamic performance of the prototype system, including in-phase and out-of-phase sine waves sound field within a short period of time, wide-band noise with a linear amplitude-in-dB envelope, and stereo playback of a song clip of "In My Life" by The Beatles (chosen because the instruments and vocals were panned to hard left or hard right owing to the audio recording and mixing technology in the 60s). The system visualizes the sound pressure of the reconstruction plane dynamically with an FPS of 62.5, offering a smooth visual effect. Because of the limitations of paper publication, we captured some results as GIF on a web which you can access in the link [15].

5   Conclusion

A DSP-based real-time sound field visualization system using SONAH algorithm is implemented. The prototype system is capable of visualizing the sound pressure distribution of the reconstruction plane in real-time. Computer simulation and free-field experiments have demonstrated that the prototype system is capable to visualize the sound field and locate the sound source within the cutoff frequency, also gains some extension ability to perform beyond the frequency range.

Further work will include refining the current system for better performance and extending the reconstruction plane from the holography plane. Other methods to solve Eq. (7) will also be implemented to remove the warp-around problem caused by the discrete representation in the wave-number domain. Furthermore, the software on the host PC will be developed and upgraded to offer more effective features for sound field visualization as well as valid user interaction.

References

1. Steiner, R., Hald, J.: Near-field Acoustical Holography without the Errors and Limitations Caused by the Use of Spatial DFT. The International Journal of Acoustics and Vibration 2(6), 834-850 (2001).
2. Cho, Y., Bolton, J., Hald, J.: Source visualization by using statistically optimized near-field acoustical holography in cylindrical coordinates. The Journal of the Acoustical Society of America 4(118), 2355-2364 (2005).
3. Li, W.: STUDY ON STATISTICALLY OPTIMAL CYLINDRICAL NEAR-FIELD ACOUSTICAL HOLOGRAPHY. Chinese Journal of Mechanical Engineering 4(41), 123 (2005).
4. Jacobsen, F., Jaud, V.: Statistically optimized near field acoustic holography using an array of pressure-velocity probes. The Journal of the Acoustical Society of America 3(121), 1550-1558 (2007).
5. Jean-Michel, F., Annie, R.: Time domain nearfield acoustical holography with three-dimensional linear deconvolution. The Journal of the Acoustical Society of America 3(143), 1672-1683 (2018).
6. Chaitanya, S. K., Thomas, S., Srinivasan, K.: Sound Source Localization using Cylindrical Nearfield Acoustic Holography. INTER-NOISE and NOISE-CON Congress and Conference Proceedings, InterNoise 18. (2018).
7. Hald, J.: Patch holography in cabin environments using a two-layer handheld array with an extended SONAH algorithm. In Proceedings of Euronoise. (2006).
8. Luo, ZW., Comesana, DF., Zheng, CJ., Bi, C.: Near-field acoustic holography with three-dimensional scanning measurements. Journal of Sound and Vibration (439), 43-55 (2019).
9. Rabinkin, D.V., Renomeron, R.J., Dahl, A.J., French, J.C., Flanagan, J.L., Bianchi, M.: A DSP implementation of source location using microphone arrays. The Journal of the Acoustical Society of America 4(99), 2503-2529 (1996).
10. Mahmod, A., Shatha, M.: TMS320C6713 DSP Kit based Hardware Implementation for the Microphone Array Beamforming System. International Journal of Computer Applications 6(179), 40-45 (2017).
11. Scholte, R.: Fourier based high-resolution near-field sound imaging. Eindhoven Technische Universiteit (2008).
12. Hald, J.: Basic theory and properties of statistically optimized near-field acoustical holography. The Journal of the Acoustical Society of America (125), 2105-2120 (2009).
13. Chen, X., Bi, C.: Jin chang sheng quan xi ji shu ji qi ying yong. Ke xue chu ban she, Beijing (2013).
14. Bi, C., Chen, X., Zhou, R., Chen, J.: Reconstruction and Separation in a Semi-Free Field by Using the Distributed Source Boundary Point Method-Based Nearfield Acoustic Holography. Journal of Vibration and Acoustics 3(129), 323 (2007).
15. Sound Field Visualization, https://zhezhang.me/2019/03/sound-field-visualization-using-sonah-algorithm, last accessed 2019/3/22.